Spontaneous and stimulated emission dynamics of PbS quantum dots in a glass matrix

Fangyu Yue
Max-Born-Institut für Nichtlineare Optik und Kurzzeitspektroskopie, Max-Born-Str. 2A, 12489 Berlin, Germany and Key Laboratory of Polar Materials and Devices, Ministry of Education, East China Normal University, Shanghai 200241, People's Republic of China

Jens W. Tomm*
Max-Born-Institut für Nichtlineare Optik und Kurzzeitspektroskopie, Max-Born-Str. 2A, 12489 Berlin, Germany

Detlef Kruschke
Institut für Angewandte Photonik e.V., Rudower Chaussee 29/31, 12489 Berlin, Germany
(Received 21 December 2012; revised manuscript received 24 April 2013; published 24 May 2013)

Optical properties and relaxation mechanisms of PbS quantum dots in glass matrix (PbS:Glass) have been systematically investigated by transmission and (steady-state and transient) photoluminescence spectroscopy. Key parameters are determined by combining the data with semiempirical expressions, based on which the recombination mechanisms including spontaneous and stimulated emissions have been discussed as a function of temperature by referring to a multilevel model including intrinsic (or *band-to-band* transition), bright, dark, and ground states. The results disclose that (i) the existence of a dark exciton state is the main reason for thermal quenching of the emission even at low temperatures due to the strong multiacoustic phonon coupling, (ii) the "intrinsic" spontaneous emission related to the intrinsic state is observed with an approximately nanosecond lifetime, in contrast to the "regular" spontaneous emission from the bright exciton state with an approximately microsecond lifetime, and (iii) stimulated emission, which has a lifetime of 20–40 ps and shows power-dependence of excitation density (or temperature), only appears from the intrinsic state but not the (bright) exciton state when enough accumulation of photogenerated carriers is reached. Furthermore, we find that the thermal conductivity will become crucial for future PbS:Glass related optoelectronic device applications.

DOI: 10.1103/PhysRevB.87.195314 PACS number(s): 78.55.Et, 81.07.Ta, 78.67.−n, 78.47.jd

I. INTRODUCTION

Semiconductor nanocrystals or quantum dots (QDs) including lead chalcogenides (e.g., PbS QDs) have been widely investigated during the past decades and still attract great attention for the potential applications in biophysics[1] and optoelectronic devices, e.g., light sources.[2,3] PbS QDs are typically embedded into colloidal or glass hosts. The latter (PbS:Glass) provides substantial advantages in terms of long-term stability. This may be decisive for future device applications. In order to design and form related devices, a systematic understanding of the optical properties of the PbS QDs is important because the QDs are not ideal two-level systems and nonradiative processes caused by the exciton fine structure are relevant.

Steady-state (SS) absorption and photoluminescence (PL), pump-probe absorption, and time-resolved (TR) PL spectroscopies have been frequently employed to investigate the optical properties of PbS QDs including the band gap (E_g) and its temperature coefficient, the QD size distribution, the (acoustic or longitudinal optical/LO) phonon energy, and the electronic fine structure as well as the carrier lifetime. For instance, the SS-absorption and emission of PbS QDs have been well described by a number of theoretical models, although an inconsistency exists among different experimental results.[4–6] At the same time, much work based on transient PL or pump-probe[7–10] has focused on the electronic or excitonic fine structure, as well as the radiative and nonradiative recombination dynamics related to spontaneous emission by referring to a model that takes into account contributions from bright and dark excitons. However, there still no decisive conclusion about the dark state, e.g., does the dark state really show radiative recombination and/or how "dark" is the dark state? As we know, the dark state has a total angular momentum of 2 and contributes to the fine structure of the exciton ground state. In contrast to bright excitons that have total angular momentum 1, dark excitons cannot recombine directly via electric dipole transitions. Although the dark state itself has been reported to radiatively relax at low temperatures (e.g., by releasing phonons), slow radiative recombination does take place since the dark exciton can undergo a thermal activation (or spin-flip) process thereby transferring into the bright state.[11,12] Furthermore, few reports address the relaxation dynamics (especially for the fast recombination process) if the excitation is increased by several orders of magnitude as compared to that in the regular spontaneous emission measurement, e.g., for investigating lasing from this kind of material.[13] Note that fast recombination at high densities (such as Auger process) has been mainly addressed for PbSe QDs.[14–16]

In this work, we employ optical spectroscopy including transmission and SS-/TR-PL to systematically investigate the optical properties and the relaxation mechanisms in PbS:Glass with a radius R of ∼2.55 nm. Key parameters have been comparatively determined according to semiempirical expressions, based on which the spontaneous emission and the stimulated emission are discussed under different experimental conditions. This work is organized as follows. After characterizing the key parameters of the QDs, we focus on the "regular"

spontaneous emission at low excitation densities as a function of temperature. Then we come to the stimulated emission and the accompanied "intrinsic" spontaneous emission under high-excitation conditions. We find that the recombination process in PbS:Glass can be modeled by a multilevel system by considering the activation of phonons, especially acoustic phonons (including absorption and release). Lattice heating (e.g., absorption of phonons) also acts as an obstacle limiting the applications in the high-power range.

II. EXPERIMENTAL DETAILS

The PbS:Glass samples were grown as described in details elsewhere[17] with the following compositions: SiO_2: 59.1, Al_2O_3: 4.2, Na_2O: 11.5, NaF: 4.3, ZnO: 11.5, ZnS: 4.0, PbO: 2.9, PbS: 1.0, with percentage of mass. A two-stage process of 475 °C/23 h plus 525 °C/1.5 h was employed for annealing. Sample plates were prepared with different thicknesses from 150 μm to 3.5 mm and were optically polished on both sides before measurements.

Transmittance was measured by a Bruker IFS-66v Fourier transform infrared (FTIR) spectrometer and/or a Perkin Elmer Lambda 900 spectrophotometer. PL was measured with the FTIR under either rapid or step scan at excitation with HeCd 442 nm or YAG 1064 nm (~87 ns pulse duration and 20 kHz repetition rate). For comparison, PL was measured in two different geometries, i.e., the standard "backscattering" or reflectance PL (R-PL) and "transmission" PL (T-PL). The latter is implemented by exciting the sample on one side while collecting PL signal from the other side. Thus the T-PL spectra are affected by reabsorption processes.

Decay curves related to regular spontaneous emission at low excitation were recorded with an InGaAs photodiode connected with a 4-GHz bandwidth digital oscilloscope. 807-nm excitation from a diode laser was used at 5-kHz repetition rate and 2-μs pulse duration. The maximum pulse excitation density was ~12 W/cm^2. TR-PL was performed by using a Tsunami Ti:sapphire laser with 100-fs pulse duration and 80-MHz repetition rate at 785 nm (or frequency-doubled 392 nm), which yielded a maximum photon fluence of 1×10^{14} cm^{-2} per pulse (or 8×10^{12} cm^{-2} per pulse for 392 nm). The detection was done by a Hamamatsu synchroscan streak camera with an S1 photocathode. The overall temporal resolution of the complete setup was better than 10 ps. The absolute PL background was cross-checked by time integrated measurements by employing a lock-in amplifier (LIA) together with a chopper and an InGaAs photodiode being incorporated into the same setup.

All measurements were done at variable temperatures by mounting the samples into the cold head of a Helium gas cycling cryogenerator. The temperature was adjusted from 5 K to ambient.

III. RESULTS AND DISCUSSION

A. Characterization by absorption and SS-PL spectra

Figure 1 shows absorption and PL spectra of a 150-μm-thick sample at 300 K. The ground-state resonance energy (for simplicity called E_g) can be determined to 1.117 eV (~1110 nm) by a Gauss-fit[18] and second-order derivative[19]

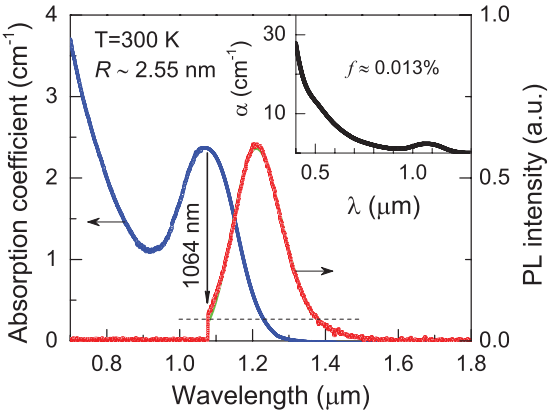

FIG. 1. (Color online) Absorption and PL spectra of a 150-μm-thick sample at 300 K. The inset gives the absorption coefficient down to as short as 400 nm. The single-Gauss fit is shown on the PL spectrum, which indicates a Stokes shift of ~93 meV (300 K).

of the absorption spectrum. The average radius R of QDs is then estimated to ~2.55 nm according to a hyperbolic-band model.[20] The maximum size variation of QDs is less than 10% as obtained by the Gaussian fit of the absorption edge.[21] The volume fraction f of the PbS QDs in the sample is ~0.013% according to the absorption coefficient at 400 nm (see the inset in Fig. 1).[4] The average distance between QDs can be estimated to ~75 nm assuming a cubic arrangement of the QDs in the matrix. Such a low f value minimizes reabsorption and energy transfer between QDs [or Förster resonance energy transfer (FRET)]. It should be noted that R-PL and T-PL performed on samples with different thicknesses also disclose a narrow size distribution of the QDs without FRET.[22] The PL spectrum, which can be well fit with a single-Gaussian function, is centered at ~1.024 eV and shows a Stokes shift of ~93 meV with respect to the resonance in absorption.

Figure 2(a) typically shows SS-PL spectra of 5, 100, and 300 K at low excitation. Note that the curves can be fit with a single-Gaussian function within the entire temperature range. The fitted results including the PL peak energy and full width at half maximum (FWHM) are summarized in Fig. 2(b). From this figure, we can see that the peak energy shows a blue shift of ~16 meV with the temperature increasing from 5 to 300 K. Based on the Varshni expression,[23] a temperature coefficient α and a Debye-temperature-related constant θ_D can be preliminarily obtained to be 59.9 ± 0.2 μeV/K and

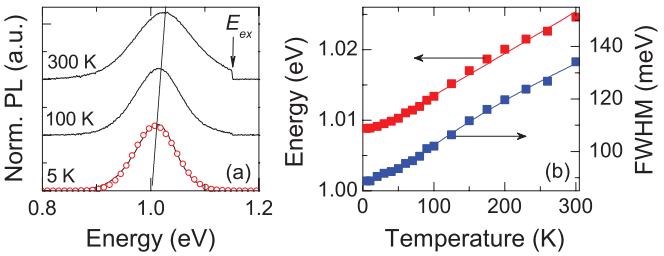

FIG. 2. (Color online) (a) SS-PL spectra at 5, 100, and 300 K. Dotted curve on the PL of 5 K is a single-Gauss fit. The solid line connecting the peaks is a guide to the eyes. E_{ex} locates the excitation energy. (b) Temperature dependence of the PL peak energy and FWHM. Solid lines are the fits described in the text.

TABLE I. Fit results of $E_g \sim T$ relationship by using Fan (or O'Donnell) formulas. "Fit" and "Calc" represent the fit and calculation values, respectively.

			S		A (meV)	
	θ_D (K)	E_p (meV)	Fit	Calc	Fit	Calc
Fan (or O'Donnell)	45.2	3.9 ± 1.4	0.346	0.868	2.7 ± 1.0	6.8
	191.2	16.5[a]	0.433	0.422	14.3	13.9
	308.1	26.6[a]	0.539	0.332	28.7	17.7

[a]Value is fixed for fitting or calculating related parameters.

20 ± 13 K, respectively. Here, the αvalue is much lower than $\sim$520 μeV/K in bulk PbS, but consistent with a theoretical estimation for PbS QDs with the same radius.[6] Note that temperature-dependent absorption data give an αvalue of $\sim$30 μeV/K, about half of that from PL spectra. A similar phenomenon has been reported before.[5,24] The fit result for θ_D is substantially smaller than the value of 145 K in bulk PbS obtained from x-ray Bragg reflection.[25] Other reports provide values in the range of 75–300 K.[26,27] It should be mentioned that other samples prepared with different annealing conditions also show low $\theta_D$values but reach maximum values of up to 82 K.

To analyze the accuracy of these parameters, we fit the experimental data with other expressions including Bose-Einstein,[28] Pässler,[29] and Fan (or O'Donnell).[30] These functions yield a consistent value of $\alpha \approx 60\,\mu$eV/K, while θ_D varies from $\sim$20 to 45 K. In addition, the Fan (or O'Donnell) gives an average phonon energy of $E_p \sim 4$ meV, much smaller than reports for the LO phonon energy of 16.5 [26,27,31] or 26.6 meV[5] in PbS QDs, but closer to the acoustic phonon energy in lead salt QD systems.[32] However, the fit parameter A (including S in O'Donnell) does not match well the calculated value from the theoretical formula,[33]

$$A = \frac{e^2}{\sqrt{2}\hbar}\sqrt{m_0 E_p}\frac{1}{4\pi\varepsilon}\left(\frac{1}{\varepsilon_\infty}-\frac{1}{\varepsilon_0}\right)\left(\sqrt{\frac{m_e}{m_0}}+\sqrt{\frac{m_h}{m_0}}\right), \quad (1)$$

where $e = 1.602\times10^{-19}$ C, $\varepsilon = 8.854\times10^{-12}$ C^2/Jm, $m_e = m_h = 0.085m_0$ (m_0 is the free electron mass), $\varepsilon_0 = 169$, and $\varepsilon_\infty = 17.2$. Table I shows the result. We point out that good agreement between the fitted and the theoretical A value (and then for S value) can be achieved by using $E_p = 16.5$ meV. The subsequently deduced θ_D, however, differs from the experimental result. For comparison, the calculated results by fixing $E_p = 26.6$ meV are also shown in Table I.

The FWHM$\sim T$ relationship [see Fig. 2(b)] gives an increase of $\sim$35 meV as the temperature rises from 5 to 300 K. It is well understood that the increasing broadening of the PL peak is mainly due to the phonon scattering. Therefore we fit the results with a function that describes the temperature dependence of the exciton peak broadening in bulk semiconductors,[34,35]

$$\mathrm{FWHM}(T) = \Gamma_{\mathrm{inh}} + \sigma T + \Gamma_{LO}\mathrm{e}^{-E_{\mathrm{LO}}/k_BT}. \quad (2)$$

Here, Γ_{inh} is the temperature-independent inhomogeneous broadening parameter, $\Gamma_{\mathrm{LO}}$is the exciton-LO phonon coupling coefficient, E_{LO} is the LO-phonon energy, σ is the exciton-acoustic phonon coupling coefficient, and k_B is the Boltzmann

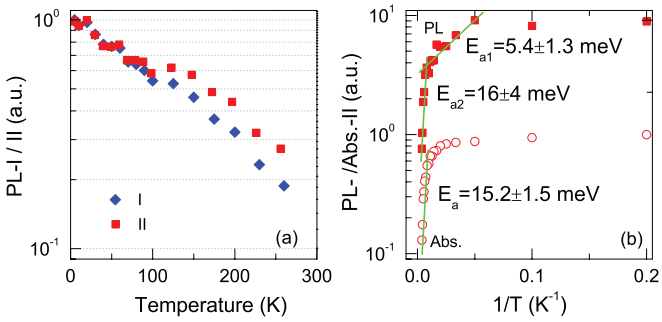

FIG. 3. (Color online) (a) Temperature dependence of PL-I and II (normalized at 300 K). (b) Arrhenius plot of PL-II together with the first absorption peak results (open dots). E_a represents the slope of related experimental data. For clarity, the data of PL-I in (a) and PL-II in (b) have been shifted.

constant. A good fit gives $\Gamma_{\mathrm{inh}} = 88.3 \pm 0.4$ meV, $\sigma = 93 \pm 12$ μeV/K, $\Gamma_{\mathrm{LO}} = 33 \pm 6$ meV, and $E_{\mathrm{LO}} = 17 \pm 1$ meV. The value Γ_{inh} matches well the result of $50 < \Gamma_{\mathrm{inh}} < 87$ meV obtained by Raman scattering.[36] Good agreement is also achieved for the LO phonon energy and the coupling coefficient of 17 and 33 meV, respectively, as reported $E_{\mathrm{LO}} = 15$ meV[5] and $\Gamma_{\mathrm{LO}} = 39 \pm 6$ meV.[9] Note that the average phonon energy obtained from Eq. (2) definitely correlates with LO phonons, in contrast to the foregoing value of $\sim$4 meV that was assumed to be driven by acoustic phonons. The σ value, however, is much higher than the scanty referable results of 54 ± 12 μeV/K ($R = 2.5$ nm)[26] and 71 ± 10 μeV/K ($R = 4.2$ nm).[24] Note also that only the three-term formula in Eq. (2), without omitting the second term σT related to the exciton-acoustic phonon interaction, can well fit the experimental data. These suggest that the acoustic phonons in the sample play a more important role in the exciton recombination process than the LO phonons.[35] Thus, they predominantly contribute to the line broadening, especially at low temperatures[32,37] [see Fig. 2(b)].

Figure 3(a) shows the PL intensity (I) and integral intensity (II) as a function of temperature (normalized at 300 K). Attention should be paid to the quenching track of PL-II (or I), namely, an approximately linear decrease rather than a slow (or exponential-like) decay[26] below $\sim$100 K followed by a discontinuity (or abnormal hop) as the temperature increases above 100 K. Shown in Fig. 3(b) is the PL-II in an Arrhenius plot from which we can see that the PL-II develops as a two-stage process including a slow decrease from 20 K and a fast one above $\sim$100 K. The slopes of these two parts can be evaluated from[38–42]

$$II_{\mathrm{norm}}(T) = (1 + B\mathrm{e}^{-E_a/k_BT})^{-1}, \quad (3)$$

where B is a fit parameter and E_a is related to the slope and can be tentatively regarded as an activation energy. The slopes can be extracted to $E_{a1} = 5.4 \pm 1.3$ meV and $E_{a2} = 16 \pm 4$ meV. For comparison, the results from the first absorption peak (Abs.-II) are also shown in Fig. 3(b). It is important to mention that almost no transition process like E_{a1} can be observed and the slope at high temperatures (above 100 K) gives a value of $E_a = 15.2 \pm 1.5$ meV, close to E_{a2} from PL results.

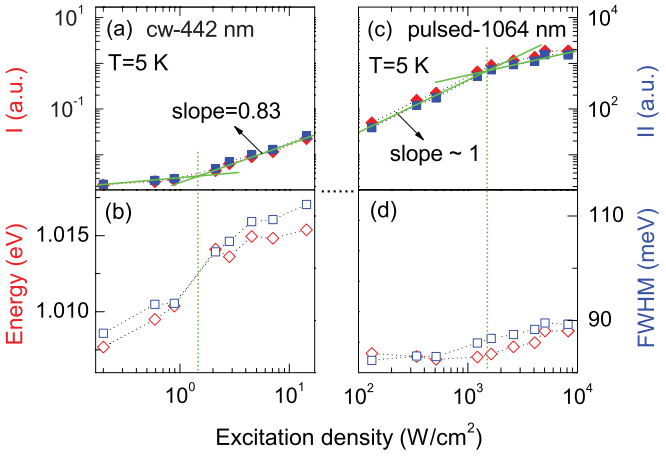

FIG. 4. (Color online) Excitation density dependence of PL-I, PL-II, peak energy and FWHM at 5 K for SS excitation at 442 nm (a) and (b) and pulsed excitation at 1064 nm (c) and (d). Note that the data in (a) and (c) [or (b) and (d)] are shown on the same scale (Red data: left axis; blue data: right axis).

Keeping in mind the intrinsic mechanism of the thermal quenching of the PL, we can infer that the nonradiative recombination (resulting in decrease of the radiative recombination) in the QDs is represented by a two-stage process. Subsequently, if we compare the activation energies obtained from PL with the foregoing phonon energies including the acoustic and LO phonons, the first rapid decrease of PL-II at low temperatures below 100 K can be attributed to the strong exciton-acoustic phonon coupling, while the second-stage quenching may be predominately caused by the exciton-LO phonon coupling at temperatures above ~100 K. Additionally, it should be pointed out that in Fig. 3(a) the nonmonotonous evolution (abnormal hop) in the range of 100–150 K suggests an increase (at least invariance) of the emission probability due to a transition from nonradiative to radiative recombination as the temperature exceeds ~100 K. Details will be discussed below.

Figure 4 summarizes the excitation density dependencies of PL-I, II, peak energy, and FWHM at 5 K. Note that the results in Figs. 4(a) and 4(b) are at SS (or cw) excitation with 442 nm, while those in Figs. 4(c) and 4(d) are obtained at pulsed excitation with 1064 nm, as described before.

We now focus on the SS excitation at excitation densities of ~W/cm^2 (left part). Figure 4(a) (on double-logarithm scale) shows that the PL-I and II increase first slowly and then rapidly as the excitation density increases. At a threshold of ~1.5 W/cm^2 (marked by vertical dash), the nearly linear increase can be fit with a slope of 0.83. Simultaneously, the peak energy and FWHM in Fig. 4(b) increase with ~8 meV and 25 meV, respectively. Therefore it can be inferred that the peak blue shift and the FWHM broadening are related to the "state filling" (what states are filled will be addressed in section 3.3) or lattice thermal effect because of the SS-excitation condition. It is necessary to mention that the existence of a threshold indicates the presence of a novel recombination mechanism increasing the radiative recombination efficiency when enough accumulation of carriers is reached.

Now we come to results obtained for pulsed excitation in Figs. 4(c) and 4(d). From Fig. 4(c), one can see that PL-I and II follow the increasing trend in Fig. 4(a) (with a slope of ~1) but then approach saturation when a critical value of ~1.5 kW/cm^2 is reached. Here, this critical value may suggest a "balance" status that the QDs in the sample are fully pumped (or excited) by the photon number of one pulse excitation (single-exciton generation tentatively assumed in individual QD). In this case, an estimate can be made by comparing the number of photons in each pulse with that of the QDs covered by the excitation beam volume, and as a result the critical excitation density can be expressed as

$$P_c = \frac{eE_{\mathrm{ex}}d_p f}{t_D V_d}, \tag{4}$$

where $E_{\mathrm{ex}} = 1.165$ eV, the pulse duration $t_D = 87$ ns, V_d is the volume of a single QD, and d_p is the penetration depth of the excitation beam into the sample and can be approximately estimated from the reciprocal of absorption coefficient[17] (~2.4 cm^{-1} at 1064 nm; see the inset in Fig. 1). The calculation gives $P_c \approx 1.7$ kW/cm^2. It is important to note that this calculated value is well in agreement with the experimentally observed changes in slopes [~1.5 kW/cm^2 in Fig. 4(c)]. This indicates that below this threshold, two subsequent pulses can be considered independent, while above carrier accumulation takes place.

Based on this discussion, it is not difficult to understand the evolutions of the peak energy and FWHM in Fig. 4(d), where they almost keep constant first and then increase separately with only ~1.5 and 6 meV as the excitation density exceeds the critical value of ~1.5 kW/cm^2. The tiny increases of peak energy and FWHM should be mainly attributed to state filling. Actually, the minor contribution from the temperature effect of E_g (or excitation-induced lattice heating) cannot be omitted if we refer to the values of E_g(30 K) ≈ 1.01 eV and E_g(300 K) ≈ 1.024 eV in Fig. 2(b). It should be pointed out that the thermal expansion coefficients of the QDs and the matrix in our samples are ~1.7×10^{-5} and 9.8×10^{-6} K^{-1}, respectively. Thus it can be taken for granted that the QDs at low temperatures (even at room temperature) are in spatially separated status from the matrix, and the blue shift of the interband (or band-related) exciton transition energy is not caused by mechanical stress.

B. Spontaneous emission at low excitation densities

Figure 5(a) shows typical decay curves of spontaneous emission ($E_{\mathrm{ex}} = 1.54$ eV) recorded at 5, 160, and 300 K, respectively. Note that a low excitation density is employed here to ensure single-exciton generation.[43,44] It is evident that the decay process is non-single-exponential (also cf. the evolution in Fig. 3), especially at low temperatures. A fit from a stretched exponential function,[45] $I(t) = \exp[(-t/\tau_{1/e})^{\beta}]$ ($0 < \beta \leqslant 1$), discloses the effective exciton lifetime τ_0 [$=\tau_{1/e}\Gamma(\beta^{-1})\beta^{-1}$, Γ is the Γ function] ranging from 2 to 11 μs (error bar ± 0.01 μs) as the temperature decreases from ambient to 5 K, which is consistent with other reports.[8,26,46,47] As shown in details in Fig. 5(b), the decay rate ($1/\tau_0$) increases first slowly and then linearly as the temperature exceeds ~90 K

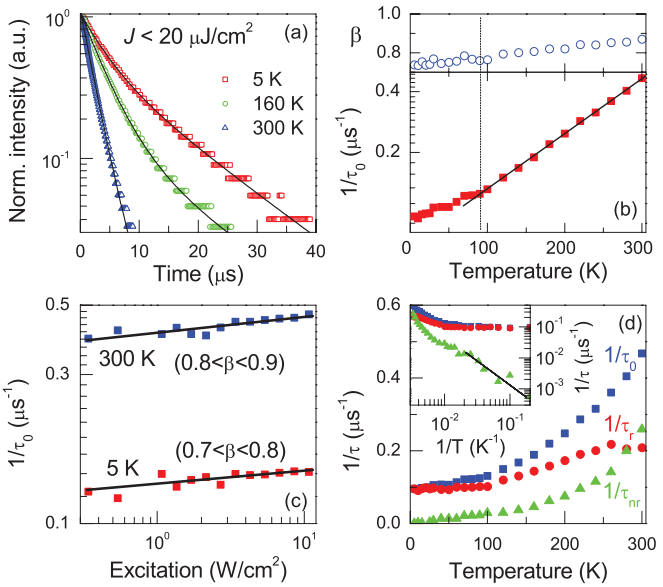

FIG. 5. (Color online) (a) Typical decay curves (5, 160, and 300 K) and fit results. (b) Temperature dependence of $1/\tau_0$ and β value. (c) Excitation density dependence of decay rates at 5 and 300 K. Linear fit yields the same slope (on double-logarithm scale). (d) Temperature dependence of the decay rates $1/\tau_i$ ($i = 0, r$, nr).

(on semilogarithmic scale) together with the β value increasing nearly linearly from 0.74 to 0.87.

Figure 5(c) gives the excitation density dependence of $1/\tau_0$ at the two extreme temperatures of 5 and 300 K, respectively. We can see that $1/\tau_0$ increases linearly with excitation density (on double-logarithm scale). This is in accordance with literature data.[48] Most important, however, is that the slopes are almost the same at the two temperatures. This illustrates that no additional relaxation mechanisms (i.e., only the approximately microsecond spontaneous emission) become effective during the whole temperature range.[8,47]

The radiative and nonradiative lifetimes as well as the quantum yield (η) can now be calculated from the following expressions by combining them with the spontaneous emission integral intensity (II_{PL}) at different temperatures,[49,50]

$$\tau_0^{-1} = \tau_r^{-1} + \tau_{\mathrm{nr}}^{-1}, \tag{5}$$

$$\eta(T) = II_{\mathrm{PL}}/II_0 = \tau_0/\tau_r. \tag{6}$$

Here, II_0 represents the PL integral intensity at 0 K. $1/\tau_r$ and $1/\tau_{\mathrm{nr}}$ are the total radiative and nonradiative recombination rates, respectively. Figure 5(d) shows the temperature dependence of $1/\tau_r$ and $1/\tau_{\mathrm{nr}}$ together with that of $1/\tau_0$. From this figure, we can see that $1/\tau_{\mathrm{nr}}$ (like $1/\tau_0$) increases nearly exponentially as the temperature increases (especially above ~100 K), while $1/\tau_r$ almost keeps first constant and then increases linearly towards saturation. For clarity, the inset gives the $(1/\tau \sim 1/T)$ relationship on a double-log scale. It is evident that the temperature has a stronger influence on the nonradiative recombination rate ($1/\tau_{\mathrm{nr}}$) at low temperatures [see the slope of the dashed line] than on $1/\tau_r$, which shows no shift as the temperature increases. Considering the low energy of the acoustic phonon (~4 meV) together with a high coupling coefficient to the exciton (~93 μeV/K) as obtained before, it can be inferred that the nonradiative recombination

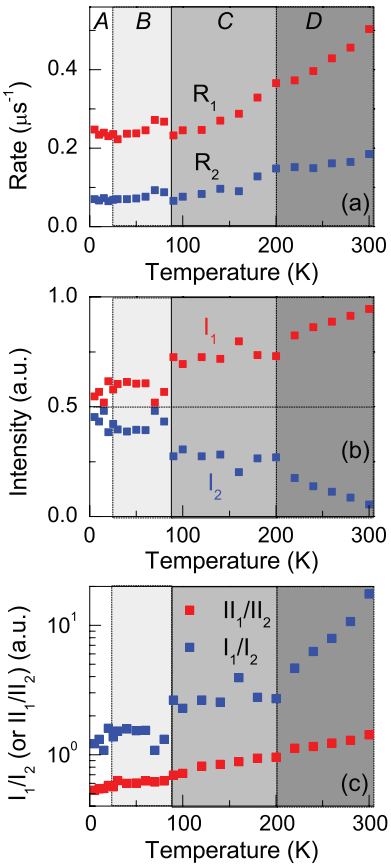

FIG. 6. (Color online) Temperature dependence of the double-exponential decay function fit results, as described in the text: (a) for decay rates R_1 and R_2, (b) for intensities (or fit amplitudes) I_1 and I_2, and (c) for the intensity ratio I_1/I_2 (or integral intensity ratio II_1/II_2). Temperature zones from A to D are shown as guide to the eyes.

at low temperatures relates to the exciton-acoustic phonon coupling.

It should be mentioned, however, that the β value is smaller than unity (0.74 ~ 0.87) even if the temperature is increased to ambient. This indicates that the decay time of the exciton ensemble has a broad distribution and suggests that more than one decay mechanism besides the radiative recombination exist during the exciton relaxation process. Therefore a double-exponential decay function is used to fit the decay curves,

$$I(t) = I_1 \exp(-t/\tau_1) + I_2 \exp(-t/\tau_2), \tag{7}$$

where I_1 and I_2 can be taken as the intensities corresponding to the fast decay rate of $1/\tau_1$ (R_1) and the comparatively slow decay rate of $1/\tau_2$ (R_2).

Figure 6 summarizes the fit results as a function of temperature. From Fig. 6(a), we can see that the two decay rates (R_1 and R_2) keep almost constant below ~90 K and then increase substantially. An evident difference between the increasing parts is visible: R_1 increases nearly exponentially, while R_2 behaves almost linearly towards saturation. Giving an analysis on Fig. 6(a), the nonmonotonous (or nonsmooth) evolution of the data indicates a multi-temperature dependent characteristic and can be roughly separated into several temperature zones: A (below ~20 K), B (20 ~ 90 K),

C (90 ~ 200 K), and D (above 200 K). This pinpoints a complex relaxation dynamics in this sample system.

Figure 6(b) gives the temperature dependence of the fit amplitude (or intensity) of the two decay rates, i.e., I_1 and I_2. It is interesting to note that the increase of I_1 mirrors the decrease of I_2 with the symmetry point located at 0.5 (i.e., the evolution center of I_1 and I_2) as the temperature increases. This suggests that at low temperatures the decay channel of R_2 mirroring predominantly nonradiative recombination has a comparable effect on the decay of exciton as R_1 but is suppressed by increasing temperature.

For clarity, Fig. 6(c) displays the value of I_1/I_2 as a function of temperature. It shows that I_1/I_2 almost exponentially increases, especially in the temperature range above 200 K. Simultaneously, a special multitemperature dependent evolution can also be observed corresponding to the A–D parts in Figs. 6(a) and 6(b). As a confirmation, the integrated intensity ratio (II_1/II_2) between R_1 and R_2 is also shown in Fig. 6(c). The nearly linear increase of II_1/II_2, illustrating that the decay relative to R_2 can be decreased by the increase of temperature as compared to R_1, suggests that a transfer exists from the R_2 decay process to the R_1 decay process as the temperature increases. Note that I_1 and I_2 are obtained from the fit of Eq. (7), while II_1 and II_2 can be inferred to be proportional to the lifetime and are deduced from

$$II_1 = \int_0^{\tau_1} \sum_{i=1,2} I_i \exp(-t/\tau_i) dt, \tag{8a}$$

$$II_2 = \int_0^{\infty} \sum_{i=1,2} I_1 \exp(-t/\tau_i) dt - II_1, \tag{8b}$$

and then the II_1/II_2 value can be calculated as below:

$$\frac{II_1}{II_2} = \frac{I_1\tau_1(1-e^{-1}) + I_2\tau_2(1-e^{-\tau_1/\tau_2})}{I_1\tau_1 e^{-1} + I_2\tau_2 e^{-\tau_1/\tau_2}}, \tag{9}$$

as shown by red squares in Fig. 6(c).

Therefore, based on the facts, (i) only a single emission peak can be observed during the entire temperature and excitation density range, (ii) the β value in dependence of temperature is obviously less than 1, (iii) PL quenches in a two-stage process as the temperature increases [see Fig. 3(b)], (iv) the phonon coupling is strong, especially the acoustic phonon coupling at low temperatures, and (v) the fast decay component increases with temperature, as compared to the slow decay component [see II_1/II_2 in Fig. 6(c)], a three-level system can be suggested to model the temperature dependence of the PL relaxation, as shown in Fig. 7. It includes an exciton ground state (G), a bright exciton state with the occupation N_B, and a dark exciton state (mainly related to nonradiative recombination) with the occupation N_D.

According to Fig. 7, the exciton relaxation process can be described within the different temperature ranges: at extremely low temperature (A, below ~20 K, $k_BT \approx 1.7$ meV), acoustic and LO phonons are almost frozen out and most of excitons decay through radiative recombination. However, nonradiative recombination caused by the existing dark state (N_D) cannot be ignored because either the βvalue is far below 1 (~0.74) or the fit amplitude of I_2, which is mainly related to the nonradiative recombination is high [also see Fig. 6(b)]. As

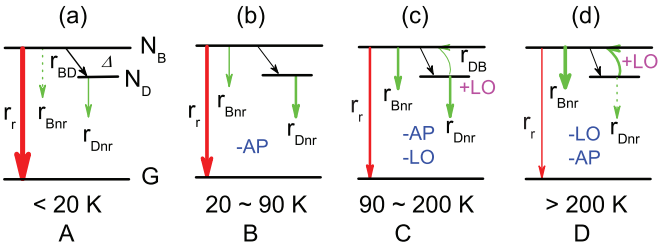

FIG. 7. (Color online) Temperature dependence of exciton relaxation dynamics on the basis of a three-level model including bright (N_B), dark (N_D), and ground (G) states. r_{BD} and r_{DB} are the relaxation and activation rates between N_B and N_D. r_r and r_{Bnr} (r_{Dnr}) separately represent the radiative and nonradiative recombination rates related to N_B (N_D). Δ is the energy difference between the dark and bright states. AP and LO represent the acoustic and LO phonon, respectively.

the temperature increases (B, 20–90 K, $k_BT \leqslant 7.8$ meV), acoustic phonons can be thermally activated ($E_{AP} \approx 4$ meV) and exciton-acoustic phonon coupling takes place with a high coupling coefficient (~93 μeV/K). This evidently decreases the PL intensity even at low temperatures [see Fig. 3(a)]. When the temperature is raised above 90 K (C zone), LO phonons ($E_{LO} \approx 16$ meV) become gradually activated due to the broad distribution of the LO phonon energy. In this case, due to the co-contribution from acoustic and LO phonon coupling the emission intensity is expected to rather decrease than being constant [see Fig. 3(a) at temperatures above ~100 K]. If we pay attention to the close value between the LO phonon energy and the activation energy deduced from Fig. 3(b), the thermal activation of the dark state (N_D) under assistance of LO phonons [with a rate of r_{DB}, see Fig. 7] is to be considered the intrinsic reason. A similar phenomenon known as a spin flip has also been reported in Refs. 51 and 52. It is worthwhile to emphasize that the increase of temperature simultaneously accelerates the nonradiative recombination (especially related to the N_B state), which dominates over the thermal activation of the N_D state. As a result, the competition between them gives a final prevailing of thermal quenching, and luminescence continuously fades away as the temperature further increases. As for the D zone (above ~200 K, $k_BT \approx 17.3$ meV) in Fig. 7 (or Fig. 6), it may correspond to the full thermal activation of the dark state [with an energy of ~16 meV; see Fig. 3(b)] by LO phonons (or multiacoustic phonons). In this case, the nonradiative recombination related to the dark state disappears and as a result the fast component becomes stronger within the temperature range over 200 K [see Fig. 6(c)]. It should be pointed out that the activation energy obtained from Eq. (3) (the larger one in Fig. 3) relates to the release (not absorption) of LO phonon, which finally leads to the rapid decrease of the emission intensity at the high temperature side.

Here, we point out that the spontaneous emission comes from the exciton state, strictly, the bright exciton state. This is the regularly investigated mechanism in the fine structure of the exciton. Thus we call it the regular spontaneous emission (briefly, SP_1), in order to differ from that in the following part.

To investigate the phonon behavior in the quenching process and to further confirm the above interpretation, in particular the existence of r_{BD} even at low temperatures, a rate equation

model based on Fig. 7 is presented to simulate the relaxation process within the three-level system. The relaxation rates of excitons located in the bright and dark states can be described by the following equations:[53]

$$\begin{aligned} \frac{dN_B}{dt} &= -N_B(r_r + r_{B\mathrm{nr}} + r_{BD}) + N_D r_{DB}, \\ \frac{dN_D}{dt} &= -N_{\mathrm{D}}(r_{D\mathrm{nr}} + r_{DB}) + N_B r_{BD}. \end{aligned} \tag{10}$$

Details of the parameters are referred to the caption of Fig. 7. The solution to the rate equations reads a double-exponential decay of $N_B(t) = I_1 e^{-R_1 t} + I_2 e^{-R_2 t}$ [like Eq. (7)], where $R_{1,2} = (A \pm \sqrt{B})/2$, and

$$A = R_1 + R_2 = r_r + r_{B\mathrm{nr}} + r_{BD} + r_{D\mathrm{nr}} + r_{DB}, \tag{11a}$$

$$B = (r_r + r_{B\mathrm{nr}} - r_{D\mathrm{nr}})^2 + 2(r_{BD} - r_{DB})(r_r + r_{B\mathrm{nr}} - r_{D\mathrm{nr}}) + (r_{BD} + r_{DB})^2, \tag{11b}$$

$$I_1 = N_{B(0)} \frac{r_r + r_{BD} + r_{\mathrm{nr}} - R_2}{R_1 - R_2} - N_{D(0)} \frac{r_{DB}}{R_1 - R_2}, \tag{11c}$$

$$I_2 = -N_{B(0)} \frac{r_r + r_{BD} + r_{\mathrm{nr}} - R_1}{R_1 - R_2} + N_{D(0)} \frac{r_{DB}}{R_1 - R_2}. \tag{11d}$$

Here, $r_{B\mathrm{nr}}$ and $r_{D\mathrm{nr}}$ can be expressed as $r_{B\mathrm{nr}} = r_0[\exp(E_p/k_BT) - 1]^{-n}$ and $r_{D\mathrm{nr}} = r_0[\exp(E_p/k_BT) - 1]^{-m}$ due to the phonon coupling with the number of n and m corresponding to the bright and dark states, respectively. $N_{B(0)}$ and $N_{D(0)}$ are the initial photogenerated exciton numbers related to the N_B and N_D states, respectively. r_0 is a temperature-independent constant. At a given temperature (or steady state), the "spin-flip" rates can be described according to the Boltzmann distribution,[54]

$$r_{BD} = r_0/(e^{\Delta/k_BT} - 1) + r_0, \tag{12a}$$

$$r_{DB} \propto r_{BD} e^{(-\Delta/k_BT)}. \tag{12b}$$

Here, Δ is the energy difference between N_B and N_D [see Fig. 7]. Note that the constant r_0 in Eq. (12a) cannot be ignored. It describes the evident nonradiative recombination even at the lowest temperature [see Fig. 6(b)].

In view of the complication of R_1, R_2, I_1, and I_2, we deduce the expressions related to decay time and relative intensity as below by assuming $N_{B(0)} = N_{D(0)}$:[53]

$$\begin{aligned} R_1 + R_2 &= r_r + r_{B\mathrm{nr}} + r_{D\mathrm{nr}} + r_{BD} + r_{DB} \\ &= r_r + r_0'[\exp(\overline{E}_p/k_BT) - 1]^{-k} \\ &\quad + r_0\{1 + 2/[\exp(\Delta/k_BT) - 1]\}, \end{aligned} \tag{13}$$

$$\frac{I_1}{I_2} = \frac{R_2 - (r_r + r_{nr} + r_0)}{r_r + r_{nr} + r_0 - R_1}, \tag{14}$$

where r_0' is a temperature-independent constant and $\overline{E}_p$ represents the average phonon energy including the contributions from acoustic and LO phonons with an average phonon number of k.

Note that the radiative contribution from the dark state in our sample system can be neglected, and that the r_r value should be dependent on temperature as deduced in Fig. 5(d), although it was presumed as a constant in the fit process in other models.[26] Thus we calculate the values of $R_1 + R_2 - r_r$ (not just $R_1 + R_2$) as a function of temperature.

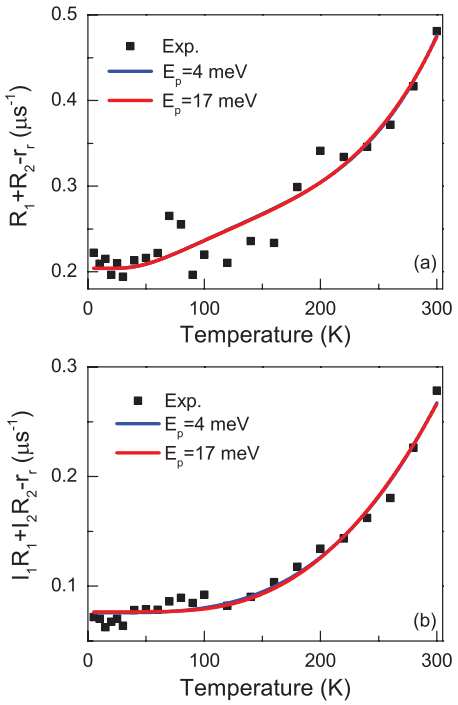

FIG. 8. (Color online) Temperature dependence of the deduced $(R_1 + R_2 - r_r)$ (a) and $(I_1R_1 + I_2R_2 - r_r)$ (b) together with the fit results, as described in the text.

Figure 8(a) shows the relationship of $(R_1 + R_2 - r_r) \sim T$, which should intrinsically follow the evolution of the nonradiative recombination related to the bright and dark states, as described in Eq. (10). The fit results are given in Fig. 8(a) by fixing $\Delta = 16$ meV [see Fig. 3(b)]. It is important to mention that the fit track is almost the same but with different phonon numbers and corresponding nonradiative recombination rates when we shift the fit value of $\overline{E}_p$ from 4 meV (close to acoustic phonon energy) to 17 meV (close to LO phonon energy), namely, $k = 4.8 \pm 1.3$ and $r_{\mathrm{nr}} = 3.17 \times 10^{-5}$ $\mu\mathrm{s}^{-1}$ for $\overline{E}_p =$ 4 meV, and $k = 3.6 \pm 1.0$ and $r_{\mathrm{nr}} = 0.12$ $\mu\mathrm{s}^{-1}$ for $\overline{E}_p =$ 17 meV. This demonstrates that the phonons own a broad energy distribution in this system, and the acoustic phonon indeed plays a key role in the thermal quenching of the spontaneous emission, since the coupling of LO phonons with a higher energy can be treated as the sum of the multiacoustic phonon coupling effect.

Simultaneously, we deduce the value of $I_1R_1 + I_2R_2$ (but not I_1/I_2) from Eq. (14) (note that $I_1 + I_2 = 1$) as $(I_1R_1 + I_2R_2) = r_r + r_{\mathrm{nr}} + r_0$. Subsequently, the fit amplitude-related results can be expressed as $(I_1R_1 + I_2R_2 - r_r) \sim T$. Shown in Fig. 8(b) is the calculated value at different temperatures together with the fit result. The fit gives an average phonon number of $k = 3.0 \pm 0.2$ and $k = 2.3 \pm 0.2$ by fixing $\overline{E}_p = 4$ and 17 meV, respectively. Comparing with the results in Fig. 8(a), one can see that the two fits give very similar numbers of phonons, confirming the presence of multiphonon coupling in the exciton relaxation process.

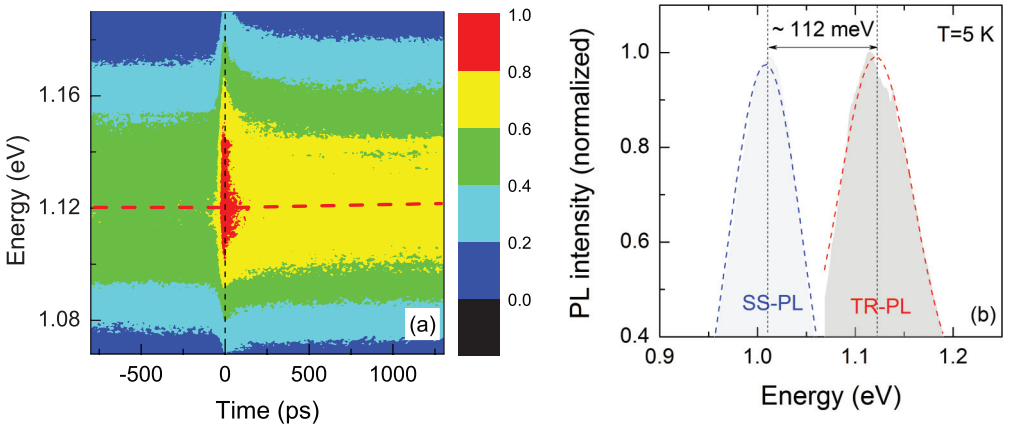

FIG. 9. (Color online) (a) Representative transient PL data at 5 K at pulsed-excitation with 785 nm. The dashed line located at ∼1.12 eV represents the emission peak position. (b) Time-integrated PL spectrum from (a) together with the SS-PL spectrum at 5 K. Dashed curves are Gauss-fit results.

C. Stimulated emission at high excitation densities

Stimulated emission can take place in this kind of material system at orders of magnitude higher excitation density as compared to that in spontaneous emission.[55] In this section, we will address the mechanisms of stimulated emission and the accompanied spontaneous emission as well as the influence of excitation density and/or temperature on the recombination.

Figure 9(a) shows transient PL data as obtained at 5 K by pulsed excitation at 785 nm (80 MHz). It is clear that besides a fast recombination component within ∼100 ps there is a strong slow recombination component [see left part below 0 ps]. In addition, the two decay components emit almost at the same spectral position of ∼1.12 eV (difference <3 meV). Compared with the peak energy of the regular spontaneous emission [see Fig. 2], however, we can find that this value is obviously blue shifted. For comparison, Fig. 9(b) shows the time-integrated TR-PL spectrum from Fig. 9(a) together with the SS-PL spectrum at the same temperature (5 K). By curve fitting with a single Gaussian function, two curves give an evident energy difference of ∼112 meV. This value pinpoints that the increase of excitation density makes the emission energy of the QDs blue shift by ∼112 meV (∼10% of E_g). It should be mentioned that the blue shift cannot be caused by the excitation-induced temperature increase (or lattice heating), since in this case a temperature over 1500 K is deduced by extrapolating the $E_g \sim T$ relationship. Subsequently, the tentative reason can be ascribed to state filling (or carrier accumulation) by considering the several order higher pulsed-excitation density at the high repetition rate of 80 MHz.

Figure 10(a) shows PL decay curves at 5 K in a wide excitation density range up to 10^8 W/cm^2. It can be seen that all curves show multiexponential decays with a common shape including a fast decay component (I_f) and a slow surviving decay tail (I_t) as well as a background (I_0) [see the inset]. To determine the decay times, the curves are fit with a double-exponential decay function [see Eq. (7)] plus an offset ($I_0 + I_t$), as shown in Fig. 10(a). Here, we define the fast and slow recombination lifetimes as τ_f and τ_s, respectively, with the corresponding fit amplitude (or intensity) of I_f and I_s. The offset of ($I_0 + I_t$) is caused by the carrier accumulation over the pulse sequence from lifetimes longer than the inverse repetition rate of 80 MHz.

Figure 10(b) gives the fitted τ_f at 5 K as a function of excitation density. It is obvious that the fast τ_f shows a nonmonotonous evolution with excitation density, namely, first keeps constant at 20–40 ps in the low excitation density range (e.g., below 2×10^7 W/cm^2) and increases towards saturation (∼90 ps) as the excitation density increases. It ends up, however, with a sharp decrease as the excitation density approaches to the highest values. As we will show later, this power dependence of τ_f is due to thermal effects and the abnormal decrease at the high excitation density side is related to an excitation-induced deterioration of sample quality.

Note that the fitted τ_s shows no evident dependence of excitation density and randomly ranges from 300 to 600 ps during the entire excitation density range, possibly due to the existence of the surviving decay tail of I_t [see Fig. 9(b)]. Therefore, in order to accurately predict the possible τ_s, a fit by omitting the offset item of I_t has been operated on decay curves. Fit results have also been shown in Fig. 10(b). It is clear that the exact τ_s is on approximately nanosecond order of magnitude and shows a similar evolution as τ_f including the abrupt decrease characteristic at the high excitation density side. It is necessary to mention that this approximately nanosecond lifetime, together with its dependence of excitation density, evidently differs from those of the regular spontaneous emission (i.e., SP_1 related to the bright exciton state) with an approximately microsecond lifetime [see Figs. 5 and 7].

As we can see, the fast recombination component (τ_f) only appears at enhanced excitation density, of which the origin may be either a radiative or nonradiative recombination. For the former, the radiative recombination can be related to multiple exciton generation (MEG) or stimulated emission since the (regular) spontaneous emission from the single-exciton recombination has a three-orders longer lifetime (approximately microseconds). However, it should be emphasized that the excitation energy of 785 nm is $E_{ex} = 1.58$ eV, substantially smaller than double ($2E_g$) of the lowest

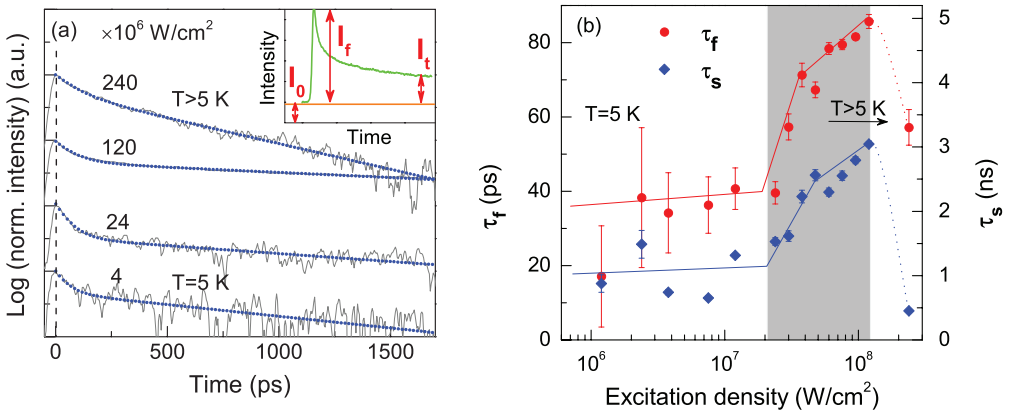

FIG. 10. (Color online) (a) Decay curves of 5 K at different pulsed excitation densities. The y axis is shown on logarithm scale. The curves are normalized and offset for clarity. The inset gives the typical characteristic of the decay curves. (b) Excitation density dependence of τ_f and τ_s. The gray zone is used as guide to the eyes.

transition energy of the QDs, i.e., $E_{\text{ex}} \approx 1.4E_g$, which should exclude radiative recombination related to MEG.[56] As for the latter (nonradiative recombination), at such high excitation density, nonlinear recombination (e.g., Auger related) may be a contribution because the phonon-assisted nonradiative recombination related to intraband (or trapping center) should be associated with a lifetime of μs order of magnitude [see Figs. 6 and 7], much longer than the obtained sub-100 ps.

Figure 11(a) shows the excitation density dependence of I_0 and I_{max} $(=I_0 + I_f)$ on a double-logarithm scale. The inset shows the I_0 data obtained from the LIA to cross-check the evolution of SS-PL signal (which can be regarded as I_0) because no fast recombination can be detected. From Fig. 11(a), as well as the inset, we can see that I_0 is strictly linear with excitation density over five orders of magnitude (on double-logarithm scale). Close to the highest excitation density, decrease can be observed. This is likely to be caused by lattice heating, since the results at excitation with the frequency-doubled 392 nm ($E_{\text{ex}} = 3.16$ eV) also show strict linearity of I_0 without appearance of the rapid decrease of I_0 for a comparatively lower excitation density (or photon number) [see also Fig. 11(a)]. Most important is that the lifetime of the fast recombination τ_f at 392 nm excitation tracks similarly as that at 785 nm but also without the rapid decrease at the highest excitation density side. Note that the excitation dependence of the emission peak energy evolves almost like that of the lifetime as shown in Fig. 10(b), namely, approximately no blue shift first as the excitation density increases from $\sim 10^6$ W/cm^2 to $\sim 2 \times 10^7$ W/cm^2 (over one order of magnitude), then a pronounced blue shift (>8 meV) appears as the excitation density increases further during the narrow gray areas [less than one order of magnitude, see Figs. 10(b) and 11]. At the highest excitation density an abrupt decrease is observed, probably due to the excitation-induced deterioration of the sample. This suggests that (i) the fast component originates from the same mechanism with the two

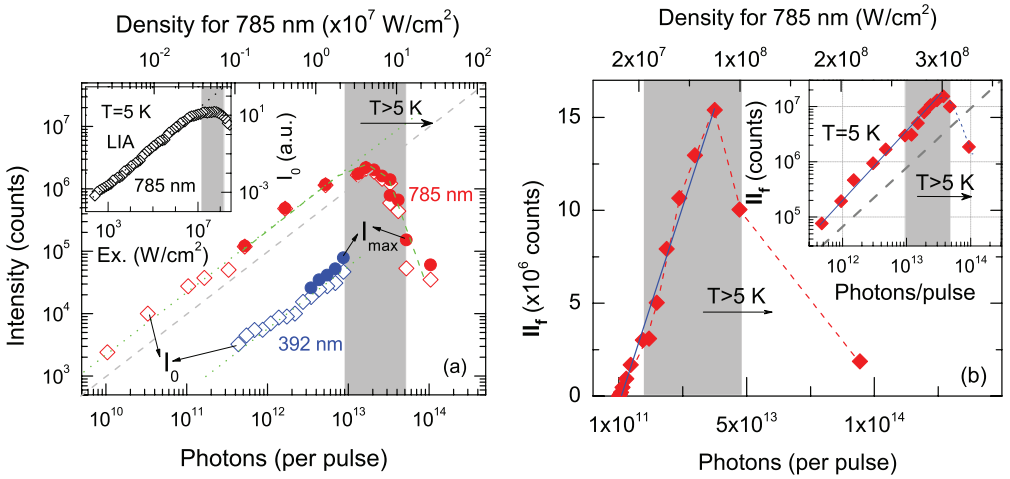

FIG. 11. (Color online) (a) Excitation density (or photon number) dependence of I_0 (open diamonds) and I_{max} (solid dots) at 5 K at excitation with 785 nm (red) and 392 nm (blue). The inset gives the absolute PL background recorded by LIA to cross-check the evolution of I_0. The gray area corresponds to the same excitation density range. (b) II_f as a function of the excitation density (or photon number) at excitation with 785 nm. The inset shows the results on double-log scale. Note that II_f (also including I_{max}) increases superlinearly, while I_0 evolves approximately linearly.

different excitation wavelengths even if the frequency-doubled excitation at 392 nm ($E_{ex} \approx 3.1E_g$) can slightly enhance the possibility of MEG and (ii) the decrease of I_0 at the high excitation density side at 785 nm is mainly caused by lattice heating. Subsequently, a preliminary conclusion can be that no nonlinear recombination (e.g., Auger-related) takes place in this excitation range, and the excitation-induced lattice heating at the high excitation density side seems to be relevant.

Note that I_f ($=I_{max}-I_0$) superlinearly increases with excitation density, although I_0 (as well as I_{max}) is decreased by lattice heating within the gray area in Fig. 11(a) (but still without deterioration of the sample quality). Similar results can be observed at 392-nm excitation. For clarity, we calculated the II_f [integral area, cf. Fig. 6(c)] as a function of excitation density (or photon number), as shown in Fig. 11(b). Here, we can see that the II_f evolves superlinearly with excitation density except for the abnormal decrease part at the highest excitation density side that has been attributed to the lattice heating as well as the deterioration of the sample quality. From this point, II_f (the fast recombination process) can be attributed to an additional radiative recombination mechanism and stimulated emission should be involved, since MEG-related radiative recombination and Auger-related nonradiative recombination have been excluded.

Above 2×10^7 W/cm^2, even the cryogenerator temperature readout shows a slight increase. Therefore the actual lattice temperature is expected to be different from the temperature readout and substantially increased. We point to this by indicating $T>5$ K, as shown in the gray areas in Figs. 10 and 11. This effect (lattice heating) explains a number of changes taking place in this excitation range: (1) τ_f and τ_s get increased with excitation density [see Fig. 10(b)]. A similar evolution related to τ_f was also observed for lasing investigation in colloidal PbS quantum dots.[13] (2) I_0 (spontaneous emission related) is substantially influenced while II_f (stimulated emission related) still superlinearly increases with excitation density [see the inset in Figs. 11(a) and 11(b)]. (3) Above the grey area (corresponding to higher excitation density) the sample quality is seriously deteriorated by the strong excitation-induced lattice heating, which makes the intensity and lifetime of the slow and fast recombination decrease rapidly.

Now we come to the temperature dependence of the exciton relaxation. Figure 12 summarizes the results including I_0, I_{max}, II_f, I_f, emission peak energy E_f, and FWHM, as well as τ_f as a function of temperature. From Fig. 12(a) we can see that I_0 (together with I_{max}) keeps constant below ~20 K. Then it decreases as the temperature increases, especially above ~100 K, where a big-step decrease appears. The characteristic of I_0 is consistent with the thermal quenching process of the spontaneous emission in Fig. 3. The evolution of I_{max} can also be used to describe the lattice heating effect in Fig. 11(a). Attention should be taken to the II_f, which increases first below 20 K and then decreases as the temperature increases further. This may be interpreted as the continuous increase (but not decrease) of II_f in Fig. 11(b) as the excitation density increases up to the grey area ($T > 5$ K due to lattice heating). However, I_f represents a nearly linear decrease during the entire temperature range (on double-log scale), as shown in Fig. 12(b).

Figure 12(c) shows the peak energy E_f and FWHM of the fast recombination. From the figure we can see that E_f increases first and then decreases with temperature. The variation of E_f is only ~3 meV, totally different from that

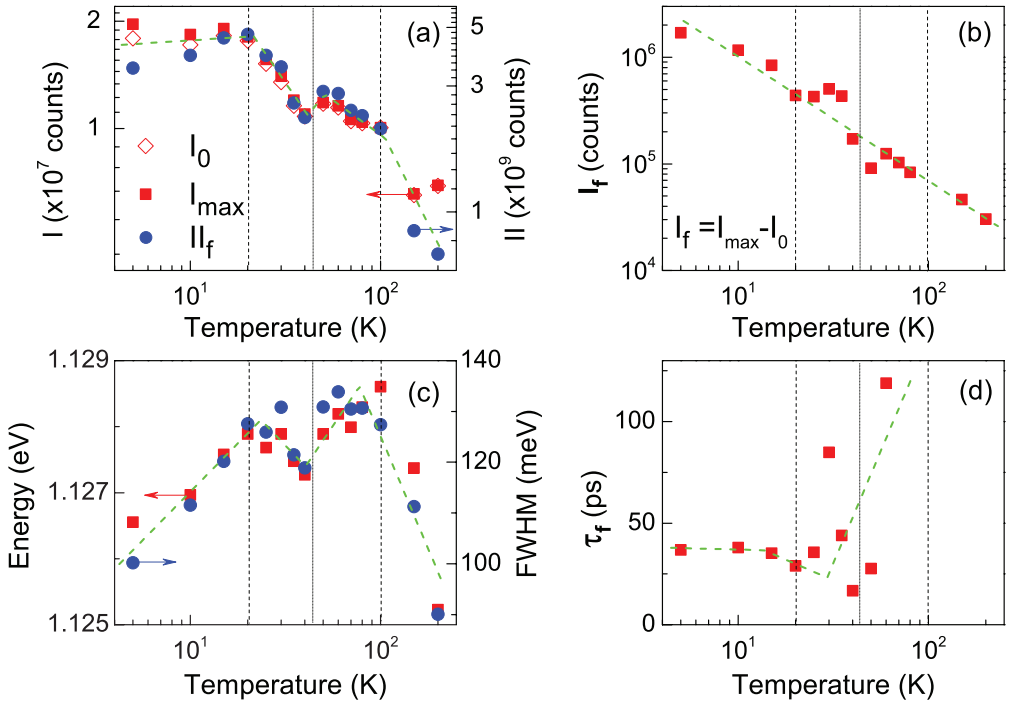

FIG. 12. (Color online) Temperature dependence of the results from decay curves including (a) I_0, I_{max}, and II_f (integral area of the fast recombination component), (b) I_f ($=I_{max}-I_0$), (c) peak energy (E_f) and FWHM of the fast recombination, and (d) τ_f.

in Fig. 2(b). Most important is the location of E_f (1.125 ∼ 1.128 eV), which is almost the same as that of the slow recombination (E_s). Thus it suggests that E_s also evolves as E_f but totally differs from the peak energy of the spontaneous emission SP_1 [see Figs. 1 and 2(b) without state filling]. Therefore the tiny variation of ∼3 meV cannot be ascribed to the temperature dependence of E_g but most likely to an increase of the kinetic energy of carriers. It is necessary to mention that the FWHM evolves like E_f and ranges from ∼90 to 135 meV (with a variation of ∼45 meV), similar to that in Fig. 2(b). Based on the foregoing discussion, the broadening of the FWHM with temperature can be attributed to the strong phonon coupling, especially the acoustic phonon coupling. As for the decrease above 200 K, it can be attributed to the deterioration of sample quality, which severely influences the emission efficiency [similar to the part as the excitation density increases into the grey area in Figs. 10(b) and 11].

Figure 12(d) gives the temperature dependence of τ_f. We can see that τ_f almost keeps constant and then increases with temperature. Note that at temperatures above 100 K decay curves still show the fast recombination component but are difficult to fit the τ_f due to the poorer signal-to-noise ratio. Back to Fig. 10(b), one can infer that lattice heating is indeed the reason for the increase of τ_f as the excitation density increases above $\sim 2\times10^7$ W/cm^2. As discussed previously, the abnormal decrease of τ_f should be caused by massive defect generation (or the deterioration of sample quality) as the temperature increases further by taking into account the rapid decrease of I_0 at the highest excitation density side in Fig. 11(a) and the temperature dependence of $I I_f$ in Fig. 12(a).

For the noncontinuous characteristics located at ∼45 K in Figs. 12(a) and 12(c), no decisive interpretation can be currently presented, although this value is very close to the Debye temperature of the material system and corresponds to the activation energy of acoustic phonons.

It should be emphasized that the slow recombination process τ_s is likely to be related to spontaneous emission. However, τ_s is on the order of nanoseconds, much shorter than that of the N_B-related (or regular) spontaneous emission (i.e., SP_1) in Fig. 7. At the same time, the emission energy of τ_s is located at the same level as that of τ_f but evidently blue shifted (∼112 meV) as compared to that of SP_1 [also see Fig. 9(b)]. Note that this blue shift is not caused by an increase in temperature. Attribution of this blue shift to excited state recombination can also be excluded because a much larger blue shift of ∼400 meV (at least ∼200 meV if the rule of optically forbidden transitions can be broken) is expected according to Refs. 6, 21, 37, and 57. Therefore a tentative assumption can be made that this blue shift, nearly close to the Stokes shift of the material at 5 K (∼120 meV), corresponds to the energy difference of the exciton (strictly bright exciton) state from the band-to-band transition (BB, here defined as the intrinsic state) by considering the excitation-induced carrier accumulation (80 MHz repetition rate) as well as the following experimental facts: (i) the correlation between lifetime and its temperature or excitation density dependencies [compare Figs. 10(b) and 5(c)]. (ii) The temperature dependence of the emission energies [compare Figs. 12(c) and 2(b)]. Note that An *et al.*[58] theoretically reported the intervalley splitting with a maximum of ∼100 meV in PbSe QDs, which may provide an explanation for this blue shift. Unfortunately, there are no comparable theoretical considerations available for the PbS:Glass system.

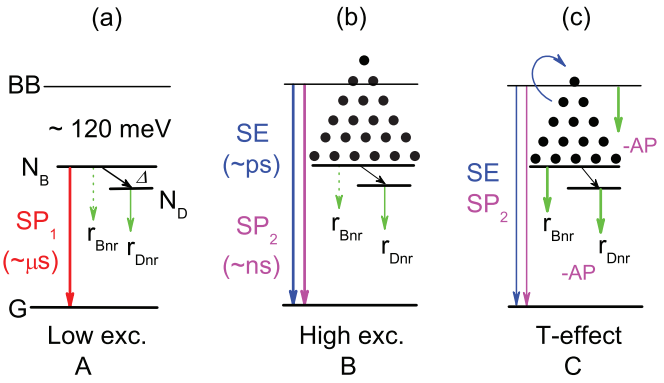

FIG. 13. (Color online) Relaxation model for different excitation conditions: (a) for low excitation, (b) for high excitation without lattice heating, where the exciton state couples to the BB state, and (c) for extremely high excitation accompanied with lattice heating (T effect). SP_1 and SP_2 represent spontaneous emission related to the bright state (approximately microsecond) and the BB state (approximately nanosecond), respectively. SE represents stimulated emission (∼30 ps). Other parameters refer to Fig. 7.

Therefore a schematic model based on the discussion for Fig. 7 is suggested to address the relaxation of excitons at different excitation densities (see Fig. 13). It is tentatively divided into three distinct excitation density ranges including A for low excitation density, B for high excitation density without lattice heating, and C for extremely high excitation density accompanied with lattice heating.

In Fig. 13(a), the excitation density is low and the photogenerated carriers decay predominantly by radiative recombination together with a minor nonradiative recombination contribution due to the existence of a dark state [see Fig. 7(a)]. Radiative recombination is only possible from the (bright) exciton-related state as spontaneous emission (i.e., SP_1) with an approximately microsecond lifetime. As the excitation density is increased by several orders of magnitude at a high repetition rate of 80 MHz (or 12.5-ns pulse cycle, three orders shorter than the SP_1 lifetime), the carriers rapidly accumulate. When the accumulation is enough for excitons to fill up to the BB level [see Fig. 13(b)] and reaches the condition of population inversion, stimulated emission takes place together with spontaneous emission (SP_2). Note that these two emissions are from the BB level but not from the N_B state [also see Fig. 7] and correspondingly a blue shift should exist with energy of $(E_{BB} - E_{N_B})$. This could be the reason why the fast and slow recombination emits at a similar energy position [see Fig. 9(a)] but with an evident blue shift compared to that of SP_1. Note also that SP_2 owns an approximately nanosecond lifetime, three orders faster than SP_1 that relates to the N_B state [see Fig. 5], and that SP_2 comes from the BB level, nominally corresponding to the intrinsic state (i.e., without Stokes shift). Thus here we call SP_2 the intrinsic spontaneous emission. As the excitation density increases further so that lattice heating appears [see Fig. 13(c)], the acoustic phonons begin to be activated, which can on the one hand increases the exciton number at the BB level by

activating the excitons from below BB to above BB, and on the other hand speeds up the nonradiative recombination by releasing acoustic phonons due to the strong exciton-acoustic phonon coupling (even at low temperature). As a result, the spontaneous emission of the BB level (maybe including the N_B level) begins to decrease although the photogenerated carrier population continues to increase with increase of excitation density [also see Figs. 9–11].

However, an interesting issue should be mentioned: the fast recombination process just appears under the condition of carrier accumulation high enough up to the BB level. This suggests that stimulated emission originates from the BB level but not from the bright exciton (N_B) state. To obtain this rigid condition, the high repetition rate of the excitation laser is essential. Otherwise, it is difficult to observe the fast process even by increasing the excitation density, since the spontaneous emissions of SP_1 with an approximately microsecond lifetime and SP_2 with an approximately nanosecond lifetime will substantially deplete excitons so that the necessary condition of population inversion can hardly be reached.

IV. CONCLUSION

PbS:Glass with $R \approx 2.55$ nm has a comparatively small temperature coefficient of E_g ($\sim$60 μeV/K) and a low Debye temperature ($\sim$45 K) as well as a strong coupling coefficient ($\sim$93 μeV/K) of exciton-acoustic phonon ($E_{AP} \approx 4$ meV) even at low temperatures as compared to that ($\sim$33 μeV/K) of exciton-LO phonon ($E_{LO} \approx 17$ meV).

By employing transient PL, the mechanisms of spontaneous and stimulated emission in PbS:Glass have been systematically discussed. The regular spontaneous emission from the bright exciton state shows an approximately microsecond lifetime, and the dynamic process with temperature can be interpreted by a three-level model by considering multiphonon coupling, especially the acoustic phonon coupling. At the same time, the intrinsic spontaneous emission from the BB level is observed with a much shorter lifetime of approximately nanosecond order of magnitude, in contrast to the regular spontaneous emission. Furthermore, stimulated emission in PbS:Glass has been found to take place from the BB level but not from the bright exciton state. The lifetime is about 20–40 ps and increases with temperature. The results of this work also suggest that improving the thermal properties of the material becomes a crucial issue for potential application of PbS:Glass in optoelectronic devices.

ACKNOWLEDGMENT

This work is supported by the BMWi-Germany (MF090215), the NSFC (60906043), and the PCSIRT and the SRFDP of China (20090076120010).

*Corresponding author: tomm@mbi-berlin.de

[1] H. Harma, J. Toivonen, J. T. Soini, P. Hanninen, and W. J. Parak, Sensors Basel **11**, 11335 (2011).
[2] E. U. Rafailov, M. A. Cataluna, and W. Sibbett, Nat. Photon. **1**, 395 (2007).
[3] T. Zhang, H. G. Zhao, D. Riabinina, M. Chaker, and D. L. Ma, J. Phys. Chem. C **114**, 10153 (2010).
[4] I. Moreels, K. Lambert, D. Smeets, D. De Muynck, T. Nollet, J. C. Martins, F. Vanhaeche, A. Vantomme, C. Delerue, G. Allan, and Z. Hens, ACS Nano **3**, 3023 (2009).
[5] B. Ullrich, J. S. Wang, and G. J. Brown, Appl. Phys. Lett. **99**, 081901 (2011).
[6] A. Olkhovets, R. C. Hsu, A. Lipovskii, and F. W. Wise, Phys. Rev. Lett. **81**, 3539 (1998).
[7] A. F. van Driel, I. S. Nikolaev, P. Vergeer, P. Lodahl, D. Vanmaekelbergh, and W. L. Vos, Phys. Rev. B **75**, 035329 (2007).
[8] M. S. Gaponenko, O. V. Buganov, A. A. Onushchenko, S. G. Hickey, A. M. Malyarevich, S. A. Tikhomirov, and K. V. Yumashev, Phys. Status Solidi (RRL) **4**, 341 (2010).
[9] G. Nair, S. M. Geyer, L. Y. Chang, and M. G. Bawendi, Phys. Rev. B **78**, 125325 (2008).
[10] K. Wundke, J. Auxier, A. Schulzgen, N. Peyghambarian, and N. F. Borrelli, Appl. Phys. Lett. **75**, 3060 (1999).
[11] S. Lüttjohann, C. Meier, M. Offer, A. Lorke, and H. Wiggers, Europhys. Lett. **79**, 37002 (2007).
[12] C. Liu, Y. K. Kwon, and J. Heo, Appl. Phys. Lett. **90**, 241111 (2007).
[13] S. Hoogland, V. Sukhovatkin, I. Howard, S. Cauchi, L. Levina, and E. H. Sargent, Opt. Express **14**, 3273 (2006).
[14] R. D. Schaller and V. I. Klimov, Phys. Rev. Lett. **92**, 186601 (2004).
[15] V. V. Klimov, A. A. Mikhailovsky, D. W. McBranch, C. A. Leatherdale, and M. G. Bawendi, Science **287**, 1011 (2000).
[16] J. M. Pietryga, K. K. Zhuravlev, M. Whitehead, V. I. Klimov, and R. D. Schaller, Phys. Rev. Lett. **101**, 217401 (2008).
[17] I. Moreels, D. Kruschke, P. Glas, and J. W. Tomm, Opt. Mater. Express **2**, 496 (2012).
[18] D. Valerini, A. Creti, M. Lomascolo, L. Manna, R. Cingolani, and M. Anni, Phys. Rev. B **71**, 235409 (2005).
[19] L. Cademartiri, E. Montanari, G. Calestani, A. Migliori, A. Guagliardi, and G. A. Ozin, J. Am. Chem. Soc. **128**, 10337 (2006).
[20] K. K. Nanda, F. E. Kruis, and H. Fissan, Nano Lett. **1**, 605 (2001).
[21] F. W. Wise, Acc. Chem. Res. **33**, 773 (2000).
[22] The symmetrical shapes of T- and R-PL remain similar as the sample thicknesses vary during a wide range from $\sim$0.15 to 3.5 mm. If reabsorption or FRET takes place, the peak energy shift and the asymmetrical shape should be evident between T- and R-PL due to the size distribution of the QDs, which has been observed in our size-graded samples.
[23] Y. P. Varshni, Physica **34**, 149 (1967).
[24] J. E. Lewis, S. Wu, and X. J. Jiang, Nanotechnology **21**, 455402 (2010).
[25] *Semiconductors: Data Handbook*, edited by M. Otfried (Springer, New York, 2004).
[26] M. S. Gaponenko, A. A. Lutich, N. A. Tolstik, A. A. Onushchenko, A. M. Malyarevich, E. P. Petrov, and K.V. Yumashev, Phys. Rev. B **82**, 125320 (2010).

[27]B. Ullrich, X. Y. Xiao, and G. J. Brown, J. Appl. Phys. **108**, 013525 (2010).
[28]L. Viña, S. Logothetidis, and M. Cardona, Phys. Rev. B **30**, 1979 (1984).
[29]R. Passler, Phys. Status Solidi B **216**, 975 (1999).
[30]K. P. O'Donnell and X. Chen, Appl. Phys. Lett. **58**, 2924 (1991).
[31]A. D. Yoffe, Adv. Phys. **50**, 1 (2001).
[32]G. I. Maikov, R. Vaxenburg, D. Yanover, A. Sashchiuk, and E. Lifshitz, Phys. Status Solidi C **7**, 2656 (2010).
[33]I. A. Vainshtein, A. F. Zatsepin, and V. S. Kortov, Phys. Solid State **41**, 905 (1999).
[34]C. Kammerer, C. Voisin, G. Cassabois, C. Delalande, P. Roussignol, F. Klopf, J. P. Reithmaier, A. Forchel, and J. M. Gerard, Phys. Rev. B **66**, 041306(R) (2002).
[35]T. D. Krauss and F. W. Wise, Phys. Rev. Lett. **79**, 5102 (1997).
[36]T. D. Krauss and F. W. Wise, Phys. Rev. B **55**, 9860 (1997).
[37]I. Kang and F. W. Wise, J. Opt. Soc. Am. B **14**, 1632 (1997).
[38]H. Sunamura, Y. Shiraki, and S. Fukatsu, Appl. Phys. Lett. **66**, 953 (1995).
[39]M. Wachter, F. Schäffler, H. J. Herzog, K. Thonke, and R. Sauer, Appl. Phys. Lett. **63**, 376 (1993).
[40]J. C. Kim, H. Rho, L. M. Smith, H. E. Jackson, S. Lee, M. Dobrowolska, and J. K. Furdyna, Appl. Phys. Lett. **75**, 214 (1999).
[41]W. I. Han, J. H. Lee, J. S. Yu, J. C. Choi, and H. S. Lee, Appl. Phys. Lett. **99**, 231908 (2011).
[42]K. C. Yew, S. F. Yoon, Z. Z. Sun, and S. Z. Wang, J. Cryst. Growth **247**, 279 (2003).
[43]V. I. Klimov, D. W. McBranch, C. A. Leatherdale, and M. G. Bawendi, Phys. Rev. B **60**, 13740 (1999).
[44]M. T. Rakher, R. Bose, C. W. Wong, and K. Srinivasan, Appl. Phys. Lett. **96**, 161108 (2010).
[45]G. Schlegel, J. Bohnenberger, I. Potapova, and A. Mews, Phys. Rev. Lett. **88**, 137401 (2002).
[46]M. S. Gaponenko, K. V. Yumashev, and A. A. Onushchenko, J. Appl. Spectrosc. **77**, 663 (2010).
[47]R. Espiau de Lamaëstre, H. Bernas, D. Pacifici, G. Franzo, and F. Priolo, Appl. Phys. Lett. **88**, 181115 (2006).
[48]C. H. Wang, T. T. Chen, Y. F. Chen, M. L. Ho, C. W. Lai, and P. T. Chou, Nanotechnology **19**, 115702 (2008).
[49]D. Fuster, J. Martínez-Pastor, L. González, and Y. González, Phys. Rev. B **71**, 205329 (2005).
[50]M. Gurioli, A. Vinattieri, M. Colocci, C. Deparis, J. Massies, G. Neu, A. Bosacchi, and S. Franchi, Phys. Rev. B **44**, 3115 (1991).
[51]J. Johansen, B. Julsgaard, S. Stobbe, J. M. Hvam, and P. Lodahl, Phys. Rev. B **81**, 081304 (2010).
[52]M. Nirmal, D. J. Norris, M. Kuno, M. G. Bawendi, Al. L. Efros, and M. Rosen, Phys. Rev. Lett. **75**, 3728 (1995).
[53]P. A. Dalgarno, J. M. Smith, B. D. Gerardot, A. O. Govorov, K. Karrai, P. M. Petroff, and R. J. Warburton, Phys. Status Solidi A **202**, 2591 (2005).
[54]R. Matsunaga, Y. Miyauchi, K. Matsuda, and Y. Kanemitsu, Phys. Rev. B **80**, 115436 (2009).
[55]F. Y. Yue, J. W. Tomm, D. Kruschke, and P. Glas, Laser Photonics Rev. **7**, L1 (2013).
[56]R. J. Ellingson, M. C. Beard, J. C. Johnson, P. Yu, O. I. Micic, A. J. Nozik, A. Shabaev, and A. L. Efros, Nano Lett. **5**, 865 (2005).
[57]N. O. Dantas, R. S. Silva, and F. Y. Qu, Phys. Status Solidi B **232**, 177 (2002).
[58]J. M. An, A. Franceschetti, and A. Zunger, Nano Lett. **7**, 2129 (2007).